Assessment of Subconjunctival Delivery with Model Ionic Permeants and Magnetic Resonance Imaging

S. Kevin Li,[1,3] Sarah A. Molokhia,[1] and Eun-Kee Jeong[2]

Received May 17, 2004; accepted August 3, 2004

Purpose. The objective was to assess the permeation and clearance of model ionic permeants after subconjunctival injection with nuclear magnetic resonance imaging (MRI).

Methods. New Zealand white rabbit was the animal model and manganese ion (Mn^{2+}) and manganese ethylenediaminetetraacetic acid complex ($MnEDTA^{2-}$) were the model permeants. The current study was divided into three parts: *in vitro*, postmortem, and *in vivo*. Transscleral passive permeation experiments were conducted with excised sclera in side-by-side diffusion cells *in vitro*. Subconjunctival delivery experiments were conducted with rabbits postmortem and *in vivo*. The distribution and elimination of the probe permeants from the subconjunctival space after subconjunctival injections were determined by MRI.

Results. The data of excised sclera *in vitro* suggest large effective pore size for transscleral transport and negligible pore charge effects upon the permeation of the ionic permeants. The permeability coefficients of Mn^{2+} and $MnEDTA^{2-}$ across the sclera *in vitro* were 3.6×10^{-5} cm/s and 2.4×10^{-5} cm/s, respectively. Although relatively high sclera permeability was observed *in vitro*, subconjunctival injections *in vivo* did not provide significant penetration of Mn^{2+} and $MnEDTA^{2-}$ into the globe; permeant concentrations in the eye were below the detection limit, which corresponds to less than 0.05% of the concentration of the injection solution (e.g., less than 0.02 mM when 40 mM injection solution was used). The volume of the subconjunctival pocket and the concentration of the permeants in the pocket were observed to decrease with time after the injection, and this could contribute to the lower than expected subconjunctival absorption *in vivo*. Different from the results *in vivo*, experiments with rabbits postmortem show significant penetration of Mn^{2+} and $MnEDTA^{2-}$ into the globe with the permeants primarily delivered into the anterior segment of the eye. This difference suggests blood vasculature clearance as a main barrier for passive transscleral transport. The data also show that the pars plicata/pars plana is the least resistance pathway for passive transscleral drug delivery of the polar permeants, and there are indications of the presence of another barrier, possibly the retinal epithelium and/or Bruch's membrane, at the back of the eye.

Conclusions. Subconjunctival delivery of the ionic permeants *in vivo* cannot be quantitatively predicted by the *in vitro* results. MRI is a noninvasive complementary technique to traditional pharmacokinetic methods. It can provide insights into ocular pharmacokinetics without permeant redistribution that can occur in surgical procedure postmortem in traditional pharmacokinetic studies when the blood vasculature barrier is absent.

KEY WORDS: Mn; MnEDTA; MRI; ocular drug delivery; subconjunctival transscleral.

[1] Pharmaceutics and Pharmaceutical Chemistry, University of Utah, Salt Lake City, Utah 84112, USA.

[2] Department of Radiology and Utah Center for Advanced Imaging Research, University of Utah, Salt Lake City, Utah 84108, USA.

[3] To whom correspondence should be addressed. (e-mail: kevin.li@m.cc.utah.edu)

INTRODUCTION

Posterior eye diseases such as intermediate and posterior uveitis, bacterial and fungal endophthalmitis, age-related macular degeneration, macular edema, viral retinitis, and diabetic retinopathy require effective drug delivery to the back of the eye for treatments. Treatments of intermediate and posterior eye diseases can be complicated due to the inaccessibility of the posterior segment of the eye to topically applied medications. Current therapies for intermediate and posterior eye diseases require repeated periocular injections, intravitreal injections, and/or high-dose systemic therapy. Injections are usually preferred to systemic drug administration because the blood-retinal barrier impedes the passage of most drugs from the systemic circulation to the interior of the eye. The large systemic doses needed to treat eye diseases often result in systemic toxicities. All these factors make drug delivery to the back of the eye a difficult task. Recently, subconjunctival injections and sustained release subconjunctival delivery systems have been proposed as potential and effective methods for drug delivery to the posterior segment of the eye (1–3).

Due to the complicated anatomy and the separated components of the eye, ocular pharmacokinetics can be complicated, and this has been reviewed in the literature (e.g., 4,5). Important aspects such as the penetration pathways and location of the barriers after subconjunctival injections are not completely clear. Previous studies on passive scleral permeability of numerous compounds *in vitro* (6–8) have shown that the transport rates of compounds with molecular weight (MW) ranging from 100 to 150,000 Daltons were relatively high and in the order of 1×10^{-6} cm/s to 1×10^{-5} cm/s. The high permeability of the sclera tissues suggests the feasibility of passive transscleral drug delivery. However, it is well known that only small amounts of drugs are found in the posterior segment of the eye after topical administration either from eye drops or ocular inserts (9). The inability to deliver drugs effectively with topical administration therefore suggests additional absorption barriers (other than the sclera) and/or conditions that hinder drug penetration. Possible absorption barriers include drug clearance of the tear film, the conjunctiva, the retinal epithelium and the blood vasculature in the conjunctiva, choroid, and retina. For example, in order for topically administered drugs to reach the vitreous and the back of the eye, the drug must pass through several layers of ocular tissues including the conjunctiva, choroid, and retina. The blood vasculature in these tissues can remove the drug, thus not allowing a significant amount of drug to reach the vitreous (10). Subconjunctival injections can bypass the conjunctiva and tear film, so factors such as drug elimination from the subconjunctival space (11–12) and blood vasculature become major determinants of the vitreous drug level after injection.

Traditional pharmacokinetic studies usually involve sacrificing animals at different time points after the administration of a compound and assaying the compound in different parts of the eye. It should be quite valuable in research to have a noninvasive approach that allows the determination of the concentration profiles of a compound in the anterior chamber, posterior chamber, and vitreous humor on a real time basis without the drawbacks of perturbation and redistribution of the compound in the eye during assay. Magnetic

resonance imaging (MRI) is such a noninvasive method that can be used to determine the distribution and route of elimination of probe ions and contrast agent labeled compounds during and after ocular delivery (13). It is a promising complementary technique to traditional pharmacokinetic methods. For example, in proton MRI, the concentration of a contrast agent (e.g., Mn^{2+}) is indirectly measured by monitoring the change in proton signal. The contrast agent enhances the relaxivity of the water protons and reduces the proton spin-lattice relaxation times (T_1). T_1 weighted MR images show enhanced signal intensities at the locations of the contrast agent. The concentration of the contrast agent in different parts of the eye (e.g., in the vitreous) can therefore be monitored.

In the current study, the permeation and clearance of model ionic permeants after subconjunctival injection was studied. Mn^{2+} and $MnEDTA^{2-}$ were the probe permeants. First, the permeability coefficients of the permeants were determined in transscleral passive permeation experiments with excised sclera in side-by-side diffusion cells *in vitro*. Then, the distribution and elimination of the probe permeants after subconjunctival administration were monitored by MRI in rabbits postmortem and *in vivo*, and compared with the data *in vitro*. The penetration pathways, the barriers, and the pharmacokinetics of the permeants in the subconjunctival space and in the eye were investigated. Important aspects of noninvasive real-time pharmacokinetic studies to avoid artifacts due to perturbation and compound redistribution in the eye during assay were also examined.

MATERIALS AND METHODS

Materials and Animals

$MnCl_2$ tetrahydrate was purchased from Spectrum Chemical (Gardena, CA, USA). Ethylenediaminetetraacetic acid (EDTA), ketamine, and xylazine were purchased from Sigma Chemical (St. Louis, MO, USA). ^{3}H-raffinose, ^{3}H-mannitol, ^{14}C-mannitol, and ^{14}C-tetraethyl ammonium (TEA) at >98% purity were purchased from New England Nuclear (Boston, MA, USA) and tested for purity using the methods specified by the supplier. 0.9% sodium chloride USP (saline, pH between 5 and 7) was from Baxter Healthcare (Deerfield, IL, USA). $Na_2MnEDTA$ solutions (with excess EDTA at 1:1 to 1:2 Mn:EDTA ratios, pH between 5 and 7) were prepared by the chemicals as received. New Zealand white rabbits of 3 to 4 kg were purchased from Western Oregon Rabbit Co. (Philomath, OR, USA) and were used as the animal model in the *in vivo* experiments under the approval of the Institutional Animal Care and Use Committee at the University of Utah. Rabbit carcasses and enucleated rabbit eyes were obtained from New Zealand white rabbits in other studies at the University of Utah Animal Resource Center.

MRI Calibration

The relationship of manganese-enhanced signal intensity vs. Mn^{2+} concentration was determined in a previous study (13). The objective of the present calibration experiments was to obtain a calibration curve of manganese-enhanced signal intensity vs. $MnEDTA^{2-}$ concentration with the $Na_2MnEDTA$ standard solutions of 0.01 to 20 mM in saline and in extracted vitreous humor. MR imaging was performed with a GE SIGNA 1.5 T (NV/CVi gradient) clinical MRI system (Milwaukee, WI, USA) (13). The MR images were analyzed using a PC with Scion Image program (Scion Corp., Frederick, MD, USA). In the experiments with rabbit vitreous humor, the vitreous humor was extracted from freshly excised eyes. Known amounts of concentrated $MnEDTA^{2-}$ solutions were then added to the vitreous humor in vials. The solutions (in capped glass vials) were imaged in a wrist coil using spin-echo pulse sequences with different repetition times (*TR*) and echo delay times (*TE*). For example, *TR* values were 200, 400, 800, 1600, and 2400 ms with *TE* fixed at 9 ms for T_1 measurements, and *TE* values were 15, 30, 45, and 60 ms with *TR* fixed at 2400 ms for the spin-spin relaxation time (T_2) measurements. Other imaging parameters were 256 readout matrix with 160 phase-encoding, 12 cm imaging field of view (*FOV*), and slice thickness of 3 mm with no spacing. The relaxation times T_1 and T_2 of these standards were determined by curve fitting of the signal intensity of a region-of-interest (ROI) with respect to the time variables *TE* and *TR* using the following spin-echo imaging equation when $TR >> TE$ (14):

$$\frac{S_1}{S_0} = (1 - e^{-TR/T_1})\, e^{-TE/T_2} \qquad (1)$$

where S_1 is the signal intensity and S_0 is the intrinsic fully-recovered signal intensity. These calibration experiments allowed us to determine the concentrations of $MnEDTA^{2-}$ by direct comparison and correct for T_2 effects at higher concentrations of the contrast agent.

Animal MRI

MRI experiments with rabbits were carried out using the same equipment as described above except that a TMJ coil (a double surface phased array coil set with 3-inch diameter) was used. Dynamic MR imaging was performed with a T_1 weighted spin-echo imaging method. Unless otherwise specified, the imaging parameters were 400 ms *TR*, 9 ms *TE*, 256 readout matrix with 160 phase-encoding, 2 signal averages to increase signal-to-noise ratio (*SNR*). The animal was in prone position (abdomen facing down) and transverse images of the head were taken. *FOV* was 12 cm with 50% or 75% *FOV* reduction factor along phase-encoding direction to reduce the imaging time. The slice thickness was 2 mm with no spacing, resulting in spatial resolution of $0.47 \times 0.47 \times 2.0$ mm^3. Prescanning was performed only once for the first data set each experiment, and the imaging parameters include the prescan results, such as transmitter and receiver gains. Imaging time for single time data was approximately 1 to 1.5 min and the temporal resolution was 4 min. The time-dependent changes of the S_1/S_0 values were used to analyze the changes in the concentration of the permeants in the aqueous and vitreous humor. All MRI experiments were carried out at least in duplicate.

From previous results (13), it should be pointed out that only the concentrations of the probe permeants in the aqueous chamber, posterior chamber, and vitreous can be quantified. The concentration in the tissues and other segments of the eye can only be described qualitatively with the present technique because of Mn^{2+}-tissue binding and the different proton relaxation times in tissues (from those in aqueous me-

dium such as aqueous humor) that can interfere with the quantification of Mn^{2+} and $MnEDTA^{2-}$ in the tissues (15–16).

In Vitro Transport Experiments

Passive permeability experiments of Mn^{2+} and $MnEDTA^{2-}$, mannitol, raffinose, and TEA were carried out with a well-stirred two-chamber side-by-side diffusion cell system with rabbit sclera. Each compartment of the diffusion cell has a 2-ml volume and an effective diffusion area of around 0.2 cm^2. The sclera tissues were obtained from both the superior and inferior temporal sections of the globe approximately 0.5 cm away from the limbus after the eye was separated from the rabbits and freed from adhering debris such as the conjunctiva and extraocular muscles. The sclera was then sandwiched between the two half-cells with the choroid side facing the receiver chamber. The diffusion cell was placed in a circulating water bath at 37 ± 1°C. Two milliliters saline and 2 ml donor solution were pipetted into the receiver and donor chambers, respectively. $MnCl_2$ (4.0 mM and 40 mM) in saline, 2.0 mM and 20 mM $Na_2MnEDTA$ (1:1 to 1:2 Mn:EDTA ratios) in saline, and trace amounts of radiolabeled mannitol, raffinose, and TEA in saline were the donor solutions. Samples were withdrawn from the donor and receiver chambers at predetermined time (20 to 60 min) intervals. Typically, 20-μl aliquots were taken from the donor chamber, and 1 ml aliquots were withdrawn from the receiver chamber. The same volume of fresh solution was added back to the receiver chamber after each aliquot removal to maintain a constant volume. The duration of the experiments was 2 to 3 h, which was at least five times longer than the transport lag time. The total permeability coefficient (P) was calculated at steady state under sink conditions (receiver concentrations ≤ 10% of the donor concentrations):

$$P = \frac{1}{C_D A_D} \frac{\Delta Q}{\Delta t} \tag{2}$$

where C_D is the concentration of the permeant in the donor chamber, A_D is the diffusional surface area, $\Delta Q/\Delta t$ is the slope of the cumulative amount of the permeant transported across the membrane into the receiver chamber vs. time plot. Transport lag time was determined by extrapolating the steady-state data in the cumulative amount vs. time plot (Q vs. t) to the abscissa. In the experiments with Mn^{2+} and $MnEDTA^{2-}$, the donor and receiver samples were analyzed by a colorimetric method. In the experiments with radiolabeled ^{3}H-mannitol, ^{14}C-mannitol, ^{3}H-raffinose, and ^{14}C-TEA, the samples were analyzed by scintillation counting.

In Vitro Experiment Assay

In the colorimetric assay for Mn^{2+} and $MnEDTA^{2-}$, the samples were mixed with 0.2 ml H_3PO_4 and 0.02 g KIO_4. The mixtures were then gently boiled for 2 to 3 min. After the vials were allowed to cool to room temperature, 0.01 g KIO_4 was added to the sample, and the samples were gently boiled again for 2 min. The samples were then diluted to 2 ml in volumetric flasks and analyzed at $\lambda = 533$ nm with a UV/Vis spectrometer (Uvikon model 810, Kontron AG, Zurich). Calibration curves were constructed with standards in a similar concentration range. For the radiolabeled permeants, the samples were mixed with 10 ml of scintillation cocktail (Ultima Gold, Packard Instrument, Meriden, CT, USA) and analyzed by a liquid scintillation counter (Packard TriCarb Model 1900TR Liquid Scintillation Analyzer).

Experiments with Rabbit Postmortem

Within one to two hours after the rabbits were sacrificed, subconjunctival injections were performed using a 30-gauge 0.5-inch needle. The site of the injection was about 3 mm away from the limbus at the center of the bulbar conjunctiva surface under the superior cul-de-sac. Briefly, the conjunctiva at the injection site was gently lifted from the surface of the globe with forceps, and the needle was tangentially inserted through the conjunctiva to deliver the permeants to the subconjunctival space without globe perforation. The upper conjunctiva was chosen because of the larger space available in the superior cul-de-sac than that in the inferior cul-de-sac of rabbits. Used in the injection were 0.1 ml of 0.4 mM, 4.0 mM, and 40 mM $MnCl_2$ in saline, 2.0 mM and 20 mM $Na_2MnEDTA$ (1:1 to 1:2 Mn:EDTA ratios) in saline, and 0.1 M $Na_2MnEDTA$ (1:1.5 Mn:EDTA ratio) in deionized water. These concentrations were selected based on the results of the MRI calibration experiments; a range of different permeant concentration was needed in the interpretation of the data and to assess permeant delivery into the eye due to the parabolic S_I/S_O vs. concentration relationships of Mn^{2+} and $MnEDTA^{2-}$ later shown in the current study. After the injection, the distribution of the probe permeants was monitored by MRI, and the concentrations of the probe permeants in the subconjunctival space, anterior chamber, posterior chamber, and vitreous were estimated by the S_I/S_O values at the ROIs and the S_I/S_O vs. concentration calibration curves.

In Vivo Experiments

After the rabbits were anesthetized with 1 mg/kg diazepam IP, 25 to 50 mg/kg ketamine IM and 5 to 10 mg/kg xylazine IM, subconjunctival injections were performed with rabbits *in vivo* using a 30-gauge 0.5-inch needle as described above. Again, the site of the needle insertion was at the center of the bulbar conjunctiva surface under the superior cul-de-sac, and 0.1 ml of 0.4 mM, 4.0 mM, and 40 mM $MnCl_2$ and 0.1 ml of 2.0 mM, 20 mM, and 0.1 M $Na_2MnEDTA$ were used. Both the left and right eyes were used in the experiments, but they were not used concurrently. The delivery and distribution of the probe permeants in the eye were monitored by MRI at least until the volume of the subconjunctival depot dropped to less than 20% of its initial subconjunctival volume or the concentration of the permeant in the subconjunctival space decreased to 20% of its original concentration. Control experiments of rabbits without any treatments to determine possible MR image artifacts were also conducted. Some animals were involved in more than one *in vivo* experiment, and they were allowed to rest for approximately one month as the washout period to recover between the experiments.

Passive Diffusion Model

Assuming a pore transport pathway model, the permeability coefficient (P) of the sclera for a permeant can be expressed as (17):

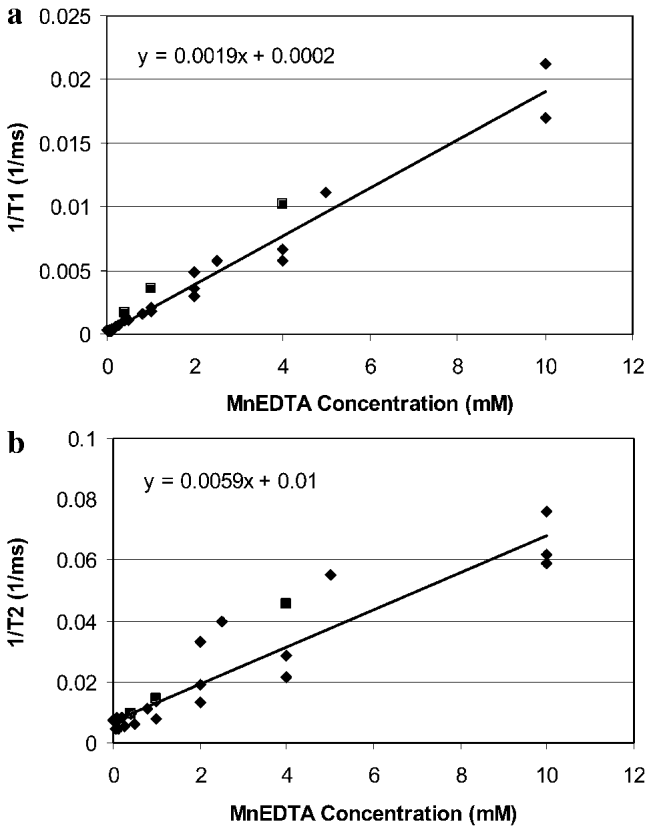

Fig. 1. (a) Relationship between the inverse of relaxation time $1/T_1$ and $MnEDTA^{2-}$ concentration. Symbols: T_1 in saline, diamonds; T_1 in vitreous humor, squares. The line is the linear least squares regression of the T_1 saline data. (b) Relationship between the inverse of relaxation time $1/T_2$ and $MnEDTA^{2-}$ concentration. Symbols: T_2 in saline, diamonds; T_2 in vitreous humor, squares. The line is the linear least squares regression of the T_2 saline data.

$$P = \frac{\varepsilon \kappa HD}{h} \tag{3}$$

where H is the hindrance transport factor, h is the effective diffusion path length (membrane thickness x tortuosity factor), ε is the membrane porosity factor, D is the free aqueous diffusion coefficient of the permeant, and κ is the ionic partition coefficient which equals unity for neutral permeants. In this model, transport lag time (T_{lag}) from the donor source across the sclera can be expressed as:

$$T_{lag} = \frac{h^2}{6HD} \tag{4}$$

Equation 3 provides the theoretical basis to analyze the permeability coefficient data of the sclera *in vitro* such as to assess possible transport hindrance and the effects of pore charge upon the transport of ionic permeants across the sclera. Equation 4 will be used later in the discussion related to the transport lag time across the sclera in the current study.

RESULTS

MRI Calibration

The relationships of the relaxation rates ($1/T_1$ and $1/T_2$) vs. the concentration of $MnEDTA^{2-}$ in saline are presented in Figs. 1a and 1b, respectively. A previous study has shown linear relationships between the relaxation rates and Mn^{2+} concentration in a similar concentration range (13). In the current study, no significant differences between the relaxation rates of $MnEDTA^{2-}$ were observed in saline and vitreous humor. Figure 2a presents the relationship between S_1/S_0 vs. the concentration of $MnEDTA^{2-}$ in saline. The relationship between S_1/S_0 and the concentration of Mn^{2+} obtained in the previous study (13) is presented in Fig. 2b. It was estimated in these figures that the detection limits of Mn^{2+} and $MnEDTA^{2-}$ in the present MRI study were approximately 0.02 mM and 0.1 mM, respectively. The data in Figs. 2a and 2b also show that the S_1/S_0 values reach a maximum of approximately 0.5 around 0.6 to 1.0 mM for Mn^{2+} and a maximum of approximately 0.7 around 3 to 5 mM for $MnEDTA^{2-}$.

Passive Permeation Across Sclera *in Vitro* and Diffusion Coefficient

The passive permeability coefficients of mannitol, raffinose, TEA, Mn^{2+}, and $MnEDTA^{2-}$ across the sclera and the donor concentrations in the experiments are presented in Table I. The diffusion coefficients of mannitol, raffinose, and TEA (17–19) are also provided in the table as references. The relatively high permeability coefficients of sclera for the permeants compared with other biologic membranes are consistent with the sclera tissue being a porous membrane composed of collagen (7). Table I also presents the transport lag

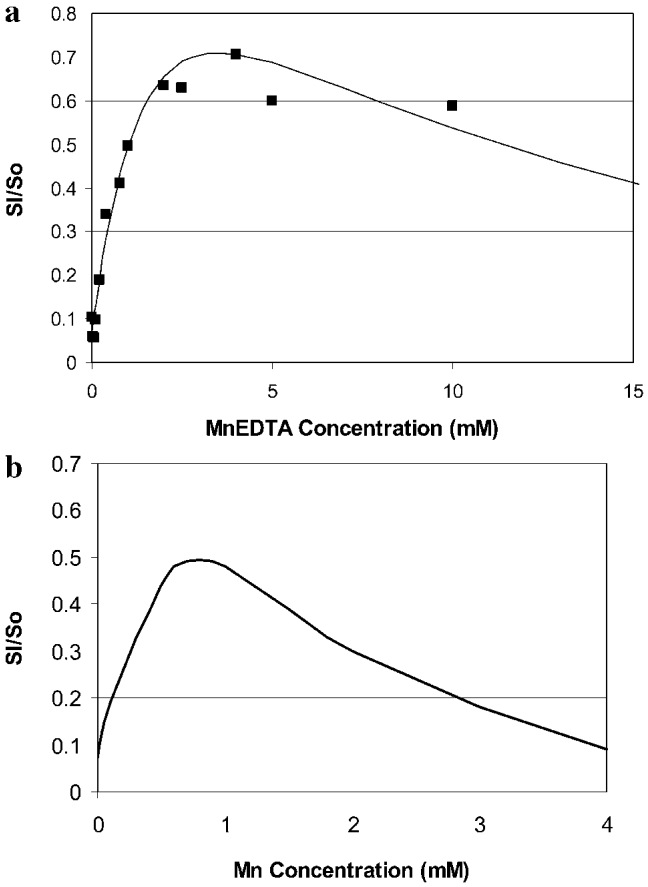

Fig. 2. (a) Relationship between signal intensity ratio S_1/S_0 and $MnEDTA^{2-}$ concentration. The curve is the least squares fitting of the data (symbols) using Eq. 1. (b) Relationship between signal intensity ratio S_1/S_0 and Mn^{2+} concentration taken from Ref. 13.

Table I. Permeability Coefficients and Lag Times of Transscleral Transport *in Vitro* and Free Aqueous Diffusion Coefficients of the Permeants

Permeant	Molecular weight	Donor concentration (mM)	Permeability coefficient[a] (10^{-5} cm/s)	Lag time (min)[a]	Diffusion coefficient from literature (10^{-5} cm^2/s)	Resulting diffusion coefficient[b] (10^{-5} cm^2/s)
Mn^{2+}	55	4	3.6 ± 0.8	14 ± 7	1.0[c]	1.3 ± 0.4
Mn^{2+}	55	40	3.4 ± 1.0	14 ± 5	1.0[c]	1.3 ± 0.4
$MnEDTA^{2-}$	343[d]	2	2.5 ± 0.1	38 ± 11		0.9 ± 0.3
$MnEDTA^{2-}$	343[d]	20	2.4 ± 0.3	19 ± 3		0.9 ± 0.3
Mannitol	182	2×10^{-5} to 5×10^{-4}[e]	2.6 ± 0.9	13 ± 6	0.90[f]	
Raffinose	504	2×10^{-5} to 2×10^{-4}[e]	1.5 ± 0.5	14 ± 6	0.57[f]	
TEA	130	0.02 to 0.1[e]	3.5 ± 0.5	8 ± 4	1.2[c]	

[a] Mean ± SD (n ≥ 3).
[b] Calculated using the ratios of the experimental permeability coefficients and literature diffusion coefficients as described in the text: $D_x = D_y P_x/P_y$, where subscripts x and y refer to permeants x and y.
[c] Data from Ref. 18 and corrected for temperature effects as described previously (17).
[d] Binding constant (K_b) of $MnEDTA^{2-}$ complex: log K_b = 13.95 in water at room temperature (38).
[e] Experiments with trace amounts of radiolabeled permeants.
[f] Data from Ref. 17.

time across the sclera for the permeants. When the concentration of the permeant ion is comparable to that of the background electrolytes (i.e., in the 40 mM $MnCl_2$ and 20 mM $Na_2MnEDTA$ experiments), migration of the permeant ion and the surrounding counterions can affect each other. In this case, the surrounding counterions and the permeant ion tend to move together to maintain electroneutrality (19). In addition, the relatively high concentration of Mn^{2+} and $MnEDTA^{2-}$ in the donor chamber in these experiments can also induce convection due to osmosis that may influence the permeability results. The data in Table I show that the permeability coefficient results are essentially the same at different donor concentrations. These results suggest minimal convention and interference from the counterions in the current transport experiments.

The permeability coefficients of mannitol, raffinose, TEA, Mn^{2+} and $MnEDTA^{2-}$ provide important insights into the barrier properties of sclera for transscleral transport. As can be seen in the table, the ratio of the permeability coefficients of mannitol and raffinose (1.7 ± 0.2) is essentially the same as their diffusion coefficient ratio (1.6). This result suggests relatively large effective pore size of the sclera for transscleral delivery and is consistent with previous finding that high molecular weight molecules can be delivered across the membrane (6). In addition, the essentially same ratio of the permeability coefficients of TEA and mannitol (1.3 ± 0.4) as that of their diffusion coefficients (1.3) indicates little pore charge effects of the sclera upon the transport of ionic permeants under the current ionic strength conditions.

With relatively unhindered transport due to the large pores of the porous structure (collagen) of sclera and without the influence of pore-to-permeant charge interactions, the free aqueous diffusion coefficients (D) of Mn^{2+} and $MnEDTA^{2-}$ can be determined by the ratio of the permeability coefficients of Mn^{2+} and mannitol (1.5 ± 0.4), the ratio of Mn^{2+} and raffinose (2.4 ± 0.6), ratio of $MnEDTA^{2-}$ and mannitol (1.0 ± 0.5), and that of $MnEDTA^{2-}$ and TEA (0.8 ± 0.1) and the literature diffusion coefficients of mannitol, raffinose, and TEA. The free diffusion coefficients of Mn^{2+} and $MnEDTA^{2-}$ determined by this method are 1.3×10^{-5} cm^2/s and 0.9×10^{-5} cm^2/s, respectively (Table I).

Experiments with Rabbit Postmortem

Figures 3 and 4 show the representative MR images after subconjunctival injections of 0.4 mM, 4.0 mM, and 40 mM $MnCl_2$ and 2 mM, 20 mM, and 0.1 M $Na_2MnEDTA$ with rabbits postmortem. Unusual eye shapes are seen in a few MR images, indicating that some eyes are slightly deformed after the animals are sacrificed. In the figures of 0.4 mM Mn^{2+} and 2 mM $MnEDTA^{2-}$, the high signal intensity spots of the subconjunctival spaces (bright areas between the upper eyelid/conjunctiva and the sclera/vitreous) can be designated as the subconjunctival depots (blebs) of Mn^{2+} and $MnEDTA^{2-}$

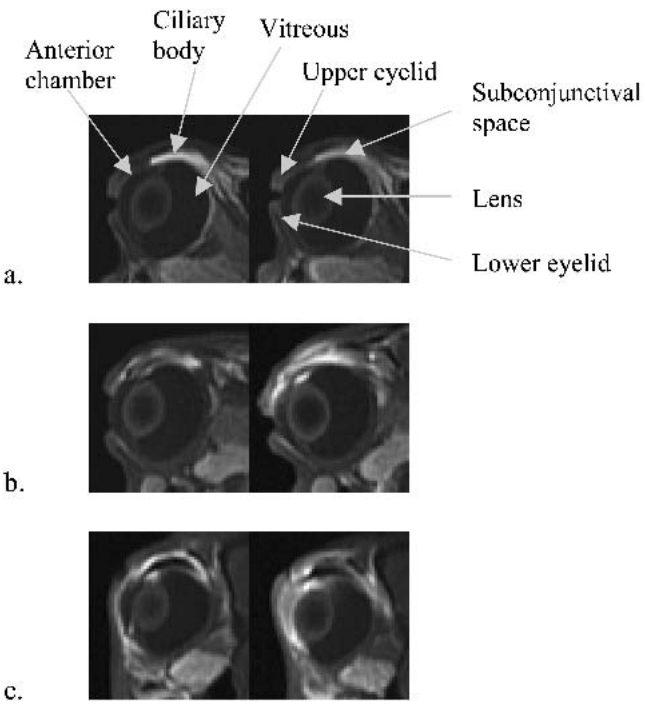

Fig. 3. Representative MR images after subconjunctival injections of (a) 0.4 mM, (b) 4 mM, and (c) 40 mM Mn^{2+} solutions postmortem. From left to right: MR images obtained at (a) 30 min, 1.8 h, (b) 24 min, 1.6 h, (c) 42 min, 1.7 h after injections.

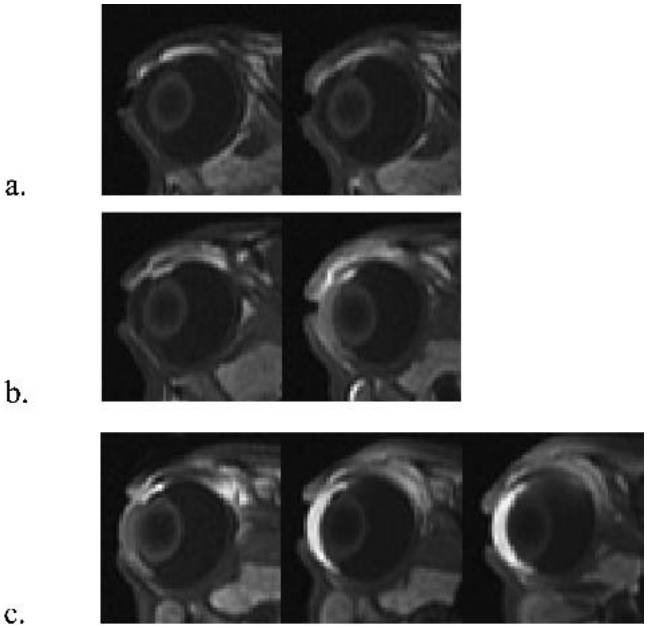

Fig. 4. Representative MR images after subconjunctival injections of (a) 2 mM, (b) 20 mM, and (c) 0.1 M $MnEDTA^{2-}$ solutions postmortem. From left to right: MR images obtained at (a) 30 min, 1.8 h, (b) 18 min, 1.8 h, (c) 31 min, 1.7 h, 2.6 h after injections.

after injections. With higher Mn^{2+} and $MnEDTA^{2-}$ concentration solutions (4 and 40 mM Mn^{2+} and 20 mM and 0.1 M $MnEDTA^{2-}$), the subconjunctival depots appear as low signal intensity areas in the subconjunctival spaces (dark areas between the upper eyelid/conjunctiva and the sclera) due to the parabolic S_I/S_O vs. concentration behaviors (see Fig. 2). Slight decreases in the concentrations of the permeants in the subconjunctival space were observed over the duration of the experiments, and the boundaries of the subconjunctival space became blurred due to the outward diffusion of the permeants. In less than one hour after subconjunctival injections of 40 mM Mn^{2+} and 0.1 M $MnEDTA^{2-}$, penetration of Mn^{2+} and $MnEDTA^{2-}$ into the ciliary body, anterior chamber, and posterior chamber near the injection site was observed (Figs. 3c and 4c). At the end of the experiment (approximately 2 h after subconjunctival injection), the anterior chamber and the posterior chamber show high MR signals with some Mn^{2+} and $MnEDTA^{2-}$ delivered into the vitreous humor in the vicinity of the subconjunctival space. Despite the high concentration in the anterior chamber, the close to the background signal intensity in the vitreous near the inferior ciliary body at 2 h after injection suggests no significant diffusion of the permeant from the anterior chamber to the vitreous in the 2-h period. In addition, the MR images of the experiments with 0.4 mM and 4 mM Mn^{2+} and 2 mM and 20 mM $MnEDTA^{2-}$ are consistent with those of 40 mM Mn^{2+} and 0.1 M $MnEDTA^{2-}$, but with less permeant penetration (Table II) due to the lower initial concentrations in the subconjunctival space.

The permeability coefficients of the permeants from the subconjunctival space into the eye can also be estimated with the MR images and Eq. 2. In this analysis, the time-dependent signal intensities of the ROIs in the anterior chamber, superior posterior chamber, and vitreous after the injections were converted to Mn^{2+} and $MnEDTA^{2-}$ concentration using the S_I/S_O vs. concentration data in Fig. 2. Then, the amounts of the permeants in these eye compartments were estimated using the concentration data and the volume of the compartments or of the ROIs (Table II). The data in Table II correspond to permeability coefficient-surface area products ($P \cdot A_D$) in the range of approximately 0.4 to 1×10^{-6} cm^3/s (estimated using Eq. 2). Because the MR images suggest that the pars plicata/pars plana is the least resistance pathway in transscleral transport postmortem (this will be discussed later), the diffusion surface area is estimated to be the area of the sclera of this pathway ($\approx$0.1 cm^2). The permeability coefficients of transscleral transport for Mn^{2+} and $MnEDTA^{2-}$ are therefore 0.4 to 1×10^{-5} cm/s. These values are lower than but in the same order of magnitude of those determined in the *in vitro* permeation experiments (Table I). Taking into account of diffusion in an unstirred system, the effects of temperature, and the uncertainty of the data, these postmortem results are consistent with the *in vitro* permeability coefficients in Table I. It should be pointed out that when 0.4 cm^2 diffusion surface (the surface area of sclera under the subconjunctival space) was used in the calculation, the permeability coefficients deter-

Table II. Amount of Permeants in the Anterior and Posterior Chambers and the Vitreous Approximately 2 h After Subconjunctival Injections with Rabbits Postmortem

		Amount (nmol)[a]					
Concentration of solution injected		Anterior and posterior chamber[b]			Vitreous[c]		
Mn^{2+}	Run	I	II	III	I	II	III
0.4 mM		ND[d]	1.0–1.5	1–3	ND[d]	ND[d]	ND[d]
4 mM		15–37	3–6	5–12	ND[d]	ND[d]	ND[d]
40 mM		75–225	60–300	120–180	1.6–2.4	1.1–2.2	2–8
$MnEDTA^{2-}$	Run	IV	V		IV	V	
2 mM		ND[d]	ND[d]		ND[d]	ND[d]	
20 mM		45–60	10–20		ND[d]	ND[d]	
0.1 M		195–270	195–285		3–4	2–3	

[a] Presented in a range, calculated from the range of concentration of the ROIs in the MR images.
[b] Volume of anterior and posterior chamber used in the calculation was 0.15 ml, estimated in the MR images.
[c] Volume of vitreous used in the calculation was the size of the ROI.
[d] Below detection limit and not determined (ND).

mined with the postmortem data will be four times lower than the 0.4 to 1 × 10^{-5} cm/s range, and this leads to further deviation from the *in vitro* permeability coefficients.

In Vivo Experiments

Figures 5 and 6 show the representative MR images after subconjunctival injections of 0.4 mM, 4.0 mM, and 40 mM $MnCl_2$ and 2 mM, 20 mM, and 0.1 M $Na_2MnEDTA$ with the rabbits *in vivo*. As can be seen in the figures, the amounts of Mn^{2+} and $MnEDTA^{2-}$ delivered into the eye after the injections were below the detection limit of the present MRI technique (0.02 mM for Mn^{2+} and 0.1 mM for $MnEDTA^{2-}$). Although the ciliary body shows a slight increase in S_t/S_o after the subconjunctival injections, the anterior chamber, posterior chamber, and vitreous show no sign of the Mn^{2+} and $MnEDTA^{2-}$ (below the detection limits) over the 2-h duration of the experiments.

Figures 5 and 6 also provide the information of the volume of the subconjunctival depot and the concentration of the permeant in the depot after injections. It should be noted that even with the same injection volume at the same injection site, variability related to the shape and the location of the subconjunctival pocket on the sclera was observed. Both the volume of the subconjunctival depot and the concentration of the permeants in the depot were observed to decrease after the injections, and the subconjunctival pocket almost completely disappeared in 2 h. Such decreases are believed to be a result of conjunctival clearance, clearance from the choroid/retina vasculature, or leakage from the subconjunctival space to the tear film and eye surface. Figure 7 shows the number of pixels of a cross-sectional area (each pixel is equivalent to 0.47 × 0.47 mm^2) of the subconjunctival pocket in the MR images at different time points after injections. From the data in the figure, the decrease in the size of the subconjunctival depot was estimated to be at a constant rate of approximately 1% of the initial volume per min. Assuming equally distributed permeants in an aqueous subconjunctival space and using the signal intensities of the subconjunctival space in the MR images at different time points, the rate of initial decrease of the subconjunctival concentration of the permeant was estimated (Fig. 8). The data from the 4 mM Mn^{2+}, 40 mM Mn^{2+}, 20 mM $MnEDTA^{2-}$, and 0.1 M $MnEDTA^{2-}$ experiments were excluded from this analysis

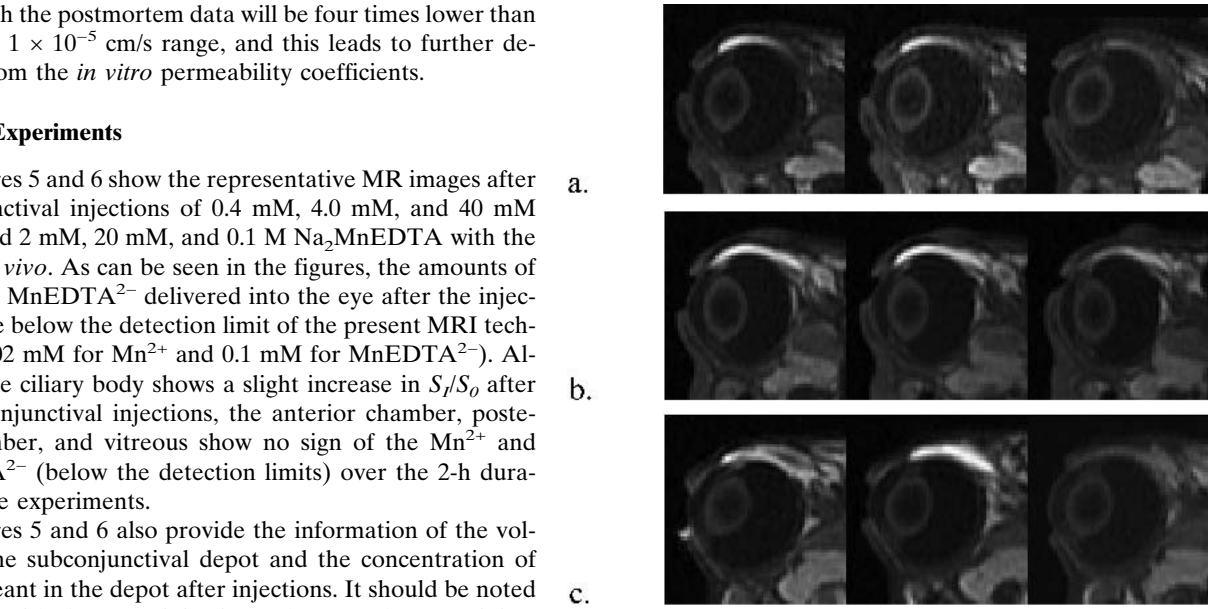

Fig. 6. Representative MR images after subconjunctival injections of (a) 2 mM, (b) 20 mM, and (c) 0.1 M $MnEDTA^{2-}$ solutions *in vivo*. From left to right: MR images obtained at (a) 15 min, 33 min, 1.4 h, (b) 17 min, 33 min, 2.1 h, (c) 14 min, 40 min, 2.0 h after injections.

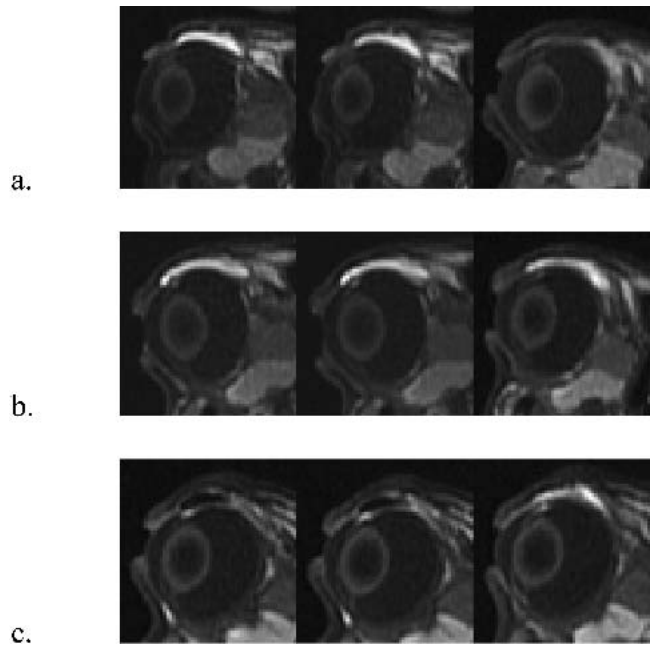

Fig. 5. Representative MR images after subconjunctival injections of (a) 0.4 mM, (b) 4 mM, and (c) 40 mM Mn^{2+} solutions *in vivo*. From left to right: MR images obtained at (a) 16 min, 31 min, 1.7 h, (b) 15 min, 30 min, 1.2 h, (c) 14 min, 31 min, 2.3 h after injections.

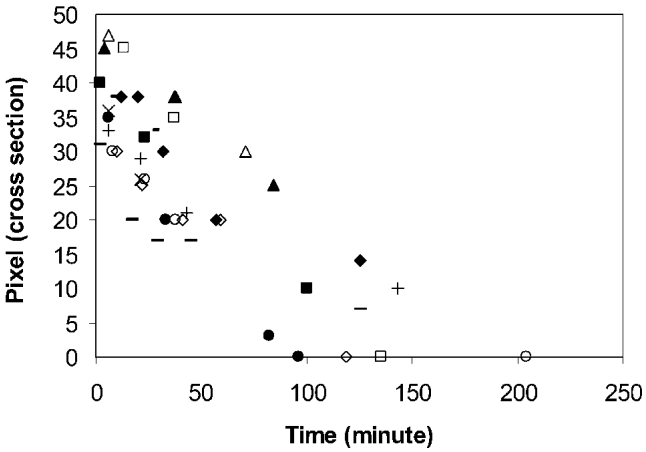

Fig. 7. Estimated cross-sectional area of the subconjunctival space in the MR images after subconjunctival injection *in vivo*. Each pixel corresponds to 0.47 × 0.47 mm^2. Significant uncertainties and errors are involved in these estimations due to the vague boundary of the subconjunctival space resulting from the penetration of the permeants into the surrounding tissues. Slopes of the least squares lines = 0.28 ± 0.14 pixel/min, corresponding to 0.8 ± 0.4%/min (mean ± SD). Each symbol represents an individually measured data point (n = 2 in each set of experiments). Symbols: 0.4 mM, 4 mM, 40 mM Mn^{2+}, squares, triangles, and crosses, respectively; 2 mM, 20 mM, 0.1 M $MnEDTA^{2-}$, circles, dashes, diamonds, respectively.

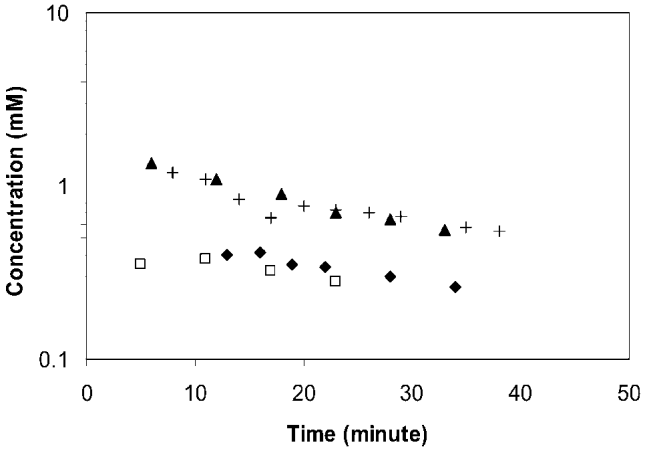

Fig. 8. Estimated concentration of Mn^{2+} and $MnEDTA^{2-}$ in the subconjunctival space after subconjunctival injection *in vivo*. Assuming first-order clearance, the rate constants (mean ± SD) calculated by the slopes of the least squares lines for Mn^{2+} and $MnEDTA^{2-}$ = 0.018 ± 0.006 min^{-1} and 0.027 ± 0.008 min^{-1}, respectively. Each symbol represents an individually calculated data point (n = 2 in each set of experiments). Symbols: 0.4 mM Mn^{2+}, squares and diamonds; 2 mM $MnEDTA^{2-}$, triangles and crosses.

because of the parabolic S_f/S_o vs. concentration relationships. In this analysis, although there was significant data scattering, the concentrations of Mn^{2+} and $MnEDTA^{2-}$ were observed to follow an approximately first-order decrease with a rate constant estimated to be around 0.0004 s^{-1}. A molecular size dependent clearance from the subconjunctival space was not observed partly due to the large data scatter and the small difference in the diffusion coefficients of Mn^{2+} and $MnEDTA^{2-}$. Both the depletion of the injection solution (volume) of the subconjunctival depot and the depletion of the permeant in the depot are substantial after the injections *in vivo*.

DISCUSSION

Absorption Barriers of Subconjunctival Injection

A main finding in the current study is the different extent of permeants delivered into the eye with the rabbits *in vivo* (Figs. 5 and 6) and those postmortem (Figs. 3 and 4) after subconjunctival injections. No significant transscleral penetration of the permeants across the barrier into the eye was observed in the experiments *in vivo*. One explanation of this is the blood vasculature clearance in the choroid being a barrier to transscleral transport *in vivo* (if the sclera and other barrier structures retain their integrity postmortem). Although not expected to be significant, intraocular pressure can also hinder the permeation of the permeants into the globe (20), and clearance by the anterior route (21,22) may contribute to the lower permeant concentration *in vivo* than postmortem. Based on the MRI detection limits of Mn^{2+} and $MnEDTA^{2-}$ and the highest concentrations used in the present subconjunctival injection study, the concentration in any parts of the eye after subconjunctival injection was less than 0.05% of the concentration of the injection solution. Considering the relatively high diffusion coefficients of Mn^{2+} and $MnEDTA^{2-}$ compared to those of the majority of ophthalmic drug molecules, subconjunctival injection is therefore not expected to achieve drug concentration higher than the 0.05% value for polar and ionic compounds. The low permeant concentration at the back of the eye after subconjunctival injection observed in the current study is also consistent with previous findings. For example, previous studies have reported that subconjunctival injections of aztreonam (23), ceftriaxone (24), pefloxacin (25), ciprofloxacin (26), cyclosporine (27), cefazolin, and cefamandole (28) can achieve only low concentrations of these compounds in the vitreous. In all cases, drug concentrations in the vitreous were found to be less than 0.05% of those in the injection solutions over the durations of these studies. Together with the data in the current study, these results suggest that passive transscleral transport can deliver sufficient amounts of drug to the back of the eye only if the minimum therapeutic concentration of the drug in the eye is low or a high injection concentration of the drug is used.

When the blood vasculature barrier is removed (postmortem rabbits), the MR images (Figs. 3 and 4) show that the route of penetration of the permeants from the subconjunctival space into the eye is near the ciliary body. This result suggests that the sclera/pars plicata and/or sclera/pars plana region provides the least resistance transport pathway for transscleral delivery of ionic permeants into the eye after subconjunctival injection. The barrier at the back of the eye is more resistive to permeation than this region; the retinal epithelium and/or Bruch's membrane may play a role as barriers to transscleral transport at the back of the eye. After the permeants penetrated the globe through this transport rate-limiting region in the postmortem rabbits, the permeants were observed to distribute primarily to the anterior segments of the eye (Figs. 3 and 4). This observation is consistent with previous studies showing that higher drug concentrations are found in the anterior chamber than in the vitreous after subconjunctival injection (26,29–31). Transport of the permeants across the cornea from the tear film into the anterior chamber was observed not to be a major route of penetration because the signal intensity patterns in the MR images indicate that most permeants diffuse from the posterior chamber (near the ciliary body) to the anterior chamber. In addition, a separate MRI passive transcorneal transport study with rabbits postmortem and *in vivo* using a passive delivery device with the same permeants at the same concentrations as those in the present study shows substantially less permeant penetration into the anterior chamber via the transcorneal route (data not shown). It should be noted that the higher permeant concentration found in the anterior chamber relative to that in the vitreous can be partly due to the differences in the volumes of the anterior chamber and the vitreous. Another possible explanation can be the gel-like properties of the vitreous humor that may create resistance to the diffusion of the permeants into the vitreous (32). However, the diffusion coefficients of ions in the vitreous humor were previously shown to be essentially the same as those of free diffusion in aqueous solution (13,33).

A semiquantitative analysis of the *in vivo* data suggests the presence of a relatively impenetrable barrier between the subconjunctival space and the vitreous that have permeability coefficients at least an order of magnitude lower than those of the sclera and retina tissues *in vitro* (10^{-5} to 10^{-4} cm/s) in the present and previous studies (7,34). For example, using the donor concentration of 40 mM, receiver concentration of 0.02 mM (the detection limit), 60 min permeation, and Eq. 2 with

the assumptions of 0.4 cm^2 diffusion surface (sclera surface under the bleb) and 1 ml receiver volume, the permeability coefficient of transscleral permeation from the subconjunctival space to the vitreous was estimated to be less than 4×10^{-7} cm/s. This value is an order of magnitude smaller than the permeability coefficients obtained in the experiments *in vitro* (Table I). In other words, if the *in vitro* permeability coefficients were used to predict the concentrations of Mn^{2+} and $MnEDTA^{2-}$ in the vitreous *in vivo*, the concentrations of the permeants in the vitreous should be at least an order of magnitude higher than the detection limits. This shows that, for the polar permeants, transscleral transport *in vivo* cannot be quantitatively predicted by experiments with excised sclera *in vitro*.

Significant decreases in both the volume of the subconjunctival depot and the concentration of the permeant in the depot were observed after subconjunctival injections *in vivo* (Figs. 7 and 8). The decreases in the subconjunctival depot volume and the permeant concentration in the depot postmortem are less than those *in vivo*. This difference is consistent with the involvement of blood vasculature in the clearance of the subconjunctival depot. The effects of permeant depletion in the subconjunctival depot upon transscleral delivery have been previously discussed (11,12). In the present study, although the decrease in the subconjunctival concentration of the permeant affects its transscleral flux, the time for 90% permeant depletion in the subconjunctival depot *in vivo* (see "Results" section) is longer than the transport lag time observed in the *in vitro* experiments (Table I). From this, the decrease in the subconjunctival concentration is expected not to reduce permeant penetration into the eye to below the detection limit for the duration of the present *in vivo* study, which is more than an order of magnitude lower than the amount of permeant expected to be delivered into the eye. If the physical properties of the sclera *in vitro* are representative to those *in vivo*, this analysis suggests that the inconsistency between the *in vitro* and *in vivo* data is related to factors such as additional tissue barriers (e.g., the retinal epithelium) and physiologic barriers (e.g., blood vasculature clearance), in addition to the influence of permeant depletion in the subconjunctival depot after subconjunctival injection.

Pharmacokinetic Studies

Due to the complicated anatomy of the eye, it is often difficult to predict the route of ocular drug delivery, pharmacokinetics, distribution, and elimination (4). Traditional pharmacokinetic studies usually involve invasive methods that can severely disturb the tissue distribution of the drug during sampling, allow drug redistribution in the eye, and require a large number of animals in each study. For example, traditional pharmacokinetic studies require sacrificing the animals at different time points after drug administration. The eyes are then enucleated and frozen immediately or treated with formaldehyde for fixation for several hours. After that, the eyes are dissected and the ocular tissues are isolated and assayed for the drug. In other studies, the aqueous or vitreous humor is aspirated by puncture with needles to assay the drug.

The current postmortem and *in vivo* results demonstrate the significance of real-time pharmacokinetic information. Once the animal is sacrificed in traditional pharmacokinetic experiments, the blood vasculature barrier ceases to exist, and drug diffusion can take place from the subconjunctival space into the eye. The results in Figs. 5c and 6c vs. those in Figs. 3c and 4c highlight this potential problem. A simple calculation using the lag time equation of the second Fick's law (e.g., Eq. 4), a diffusion coefficient of 10^{-5} cm^2/s, and an effective thickness of 0.2 cm (a tortuosity factor of three times the average combined thickness of rabbit sclera, choroid, and retina) shows that the time for the permeant to passively diffuse across the sclera is in the order of minutes. With small animals such as rats and mice, the effect of redistribution is expected to be more pronounced because of the dimensions of the sclera and other eye tissues of small animals and the nonlinear relationship between the diffusion path length and diffusion lag time (Eq. 4). For example, assuming a maximum effective thickness value of 0.05 cm in mice (sclera thickness in mice is approximately 0.005 to 0.008 cm and tortuosity factor is not known), the time for drug redistribution across the sclera is in the order of tenths of seconds. This simple analysis suggests that the experimental procedures themselves such as the time for carrying out the surgical procedures can affect the outcomes of traditional pharmacokinetic studies. Because MRI is non-invasive, it can provide real-time data for ocular delivery study without perturbation of the eye and redistribution of the permeant in the eye that can occur in traditional pharmacokinetic studies.

Although MRI has previously been used in ocular research (22,33,35,36), to our knowledge, the current study is the first to use MRI as a noninvasive method in an attempt to retrieve real-time information on the pharmacokinetics of ionic permeants in the eye after subconjunctival injection. However, it is important to note that quantitative MRI analyses at the present stage are limited to the anterior chamber, posterior chamber, and vitreous because T_1 and T_2 relaxivities of the contrast agents in tissues are complicated. Another important issue related to MRI ocular pharmacokinetic studies is the detection limits of the probe permeants in this technique. With the equipment and imaging parameters used in the current study, the detection limits in the aqueous and vitreous humors are approximately 0.02 mM and 0.1 mM for Mn^{2+} and $MnEDTA^{2-}$, respectively. These may not be sensitive enough to provide useful information in ocular pharmacokinetics because the therapeutic levels of some pharmaceutical agents are below these limits. However, the detection limit (i.e., *SNR*) can be improved with a higher magnetic field MRI system, special RF coils for ocular MRI, increasing scan time, and/or decreasing spatial resolution. Future MRI work should address this issue. Besides the detection limit and the complexity of quantifying the concentrations of the contrast agents in different tissues, the use of Mn^{2+} also poses another problem: Mn^{2+} can be taken up by the retinal ganglion cells and transported (at a rate of 0.28 cm/h) along the optic axon *in vivo* (15,16). In the current study, $MnEDTA^{2-}$ can serve as an alternative surrogate permeant to support the conclusions of the Mn^{2+} study. The consistency seen from the results of the Mn^{2+} and $MnEDTA^{2-}$ experiments (e.g., Figs. 3 to 6) suggest that the results of Mn^{2+} are not significantly affected by specific tissue-Mn^{2+} interactions. It should also be noted that the MR images obtained in the present study are consistent with a recent MRI study of ocular implant placed on the episclera using gadolinium-diethylenetriaminopentaacetic acid as the model permeant (37). The results in this recent

study reinforce the conclusions of the present study with Mn^{2+} and $MnEDTA^{2-}$.

ACKNOWLEDGMENTS

This research was supported in part by NIH grant GM063559. The authors thank Henry R. Buswell and Dr. Rajan P. Kochambilli for their help in the preparation of the experiments, Matthew S. Hastings, Dr. William I. Higuchi, Dr. Thomas W.Y. Lee, Dr. Martin J. Lizak, and Dr. Paul S. Bernstein for helpful discussion.

REFERENCES

1. T. W. Kim, J. D. Lindsey, M. Aihara, T. L. Anthony, and R. N. Weinreb. Intraocular distribution of 70-kDa dextran after subconjunctival injection in mice. *Invest. Ophthalmol. Vis. Sci.* **43**: 1809–1816 (2002).
2. Y. Yanagi, Y. Tamaki, R. Obata, K. Muranaka, N. Homma, H. Matsuoka, and H. Mano. Subconjunctival administration of bucillamine suppresses choroidal neovascularization in rat. *Invest. Ophthalmol. Vis. Sci.* **43**:3495–3499 (2002).
3. U. B. Kompella, N. Bandi, and S. P. Ayalasomayajula. Subconjunctival nano- and microparticles sustain retinal delivery of budesonide, a corticosteroid capable of inhibiting VEGF expression. *Invest. Ophthalmol. Vis. Sci.* **44**:1192–1201 (2003).
4. N. Worakul and J. R. Robinson. Ocular pharmacokinetics/pharmacodynamics. *Eur. J. Pharm. Biopharm.* **44**:71–83 (1997).
5. T. J. Zimmerman, K. S. Kooner, M. Sharir, and R. D. Fechtner. *Textbook of Ocular Pharmacology*, Lippincoot-Raven, Philadelphia, 1997.
6. D. H. Geroski and H. F. Edelhauser. Transscleral drug delivery for posterior segment disease. *Adv. Drug Deliv. Rev.* **52**:37–48 (2001).
7. M. R. Prausnitz and J. S. Noonan. Permeability of cornea, sclera, and conjunctiva: a literature analysis for drug delivery to the eye. *J. Pharm. Sci.* **87**:1479–1488 (1998).
8. J. Ambati, C. S. Canakis, J. W. Miller, E. S. Gragoudas, A. Edwards, D. J. Weissgold, I. Kim, F. C. Delori, and A. P. Adamis. Diffusion of high molecular weight compounds through sclera. *Invest. Ophthalmol. Vis. Sci.* **41**:1181–1185 (2000).
9. A. K. Mitra. *Ophthalmic Drug Delivery Systems*, Marcel Dekker, New York, 1993.
10. Y. Ogura. Drug delivery to the posterior segments of the eye. *Adv. Drug Deliv. Rev.* **52**:1–3 (2001).
11. T. W. Lee and J. R. Robinson. Drug delivery to the posterior segment of the eye II: development and validation of a simple pharmacokinetic model for subconjunctival injection. *J. Ocul. Pharmacol. Ther.* **20**:43–53 (2004).
12. T. W. Lee and J. R. Robinson. Drug delivery to the posterior segment of the eye III: the effect of parallel elimination pathway on the vitreous drug level after subconjunctival injection. *J. Ocul. Pharmacol. Ther.* **20**:55–64 (2004).
13. S. K. Li, E. K. Jeong, and M. S. Hastings. Magnetic resonance imaging study of current and ion delivery into the eye during transscleral and transcorneal iontophoresis. *Invest. Ophthalmol. Vis. Sci.* **45**:1224–1231 (2004).
14. D. D. Stark and W. G. Bradley. *Magnetic Resonance Imaging*, 2nd ed. Mosbey Year Book, Boston, 1992, Ch. 14.
15. T. Watanabe, T. Michaelis, and J. Frahm. Mapping of retinal projections in the living rat using high-resolution 3D gradient-echo MRI with Mn^{2+}-induced contrast. *Magn. Reson. Med.* **46**: 424–429 (2001).
16. R. G. Pautler, R. Mongeau, and R. E. Jacobs. In vivo trans-synaptic tract tracing from the murine striatum and amygdala utilizing manganese enhanced MRI (MEMRI). *Magn. Reson. Med.* **50**: 33–39 (2003).
17. K. D. Peck, A. H. Ghanem, and W. I. Higuchi. Hindered diffusion of polar molecules through and effective pore radii estimates of intact and ethanol treated human epidermal membrane. *Pharm. Res.* **11**:1306–1314 (1994).
18. D. R. Lide. *CRC Handbook for Chemistry and Physics*, CRC Press, New York, 2004.
19. S. K. Li, A. H. Ghanem, K. D. Peck, and W. I. Higuchi. Iontophoretic transport across a synthetic membrane and human epidermal membrane: a study of the effects of permeant charge. *J. Pharm. Sci.* **86**:680–689 (1997).
20. D. E. Rudnick, J. S. Noonan, D. H. Geroski, M. R. Prausnitz, and H. F. Edelhauser. The effect of intraocular pressure on human and rabbit scleral permeability. *Invest. Ophthalmol. Vis. Sci.* **40**: 3054–3058 (1999).
21. M. E. Yablonski, M. Hayashi, D. J. Cook, G. Chubak, and M. Sirota. Fluorophotometric study of intravenous carbonic anhydrase inhibitors in rabbits. *Invest. Ophthalmol. Vis. Sci.* **28**:2076–2082 (1987).
22. H. M. Cheng, K. K. Kwong, J. Xiong, and C. Chang. GdDTPA-enhanced magnetic resonance imaging of the aqueous flow in the rabbit eye. *Magn. Reson. Med.* **17**:237–243 (1991).
23. M. Barza and M. McCue. Pharmacokinetics of aztreonam in rabbit eyes. *Antimicrob. Agents Chemother.* **24**:468–473 (1983).
24. W. M. Jay, R. K. Shockley, A. M. Aziz, M. Z. Aziz, and J. P. Rissing. Ocular pharmacokinetics of ceftriaxone following subconjunctival injection in rabbits. *Arch. Ophthalmol.* **102**:430–432 (1984).
25. S. Marrakchi-Benjaafar, I. Cochereau, F. D'Hermies, and J. J. Pocidalo. Tolerability, kinetics, and efficacy of subconjunctival pefloxacin in pigmented rabbits. *Antimicrob. Agents Chemother.* **39**:834–838 (1995).
26. D. P. Hainsworth, J. D. Conklin, J. R. Bierly, D. Ax, and P. Ashton. Intravitreal delivery of ciprofloxacin. *J. Ocul. Pharmacol. Ther.* **12**:183–191 (1996).
27. G. S. Kalsi, G. Gudauskas, N. Bussanich, D. J. Freeman, and J. Rootman. Ocular pharmacokinetics of subconjunctivally administered cyclosporine in the rabbit. *Can. J. Ophthalmol.* **26**: 200–205 (1991).
28. M. Barza, A. Kane, and J. L. Baum. Intraocular levels of cefamandole compared with cefazolin after subconjunctival injection in rabbits. *Invest. Ophthalmol. Vis. Sci.* **18**:250–255 (1979).
29. E. F. Erkin, U. Gunenc, F. H. Oner, A. Gelal, Y. Erkin, and H. Guven. Penetration of amikacin into aqueous humor of rabbits. *Ophthalmologica* **215**:299–302 (2001).
30. M. Souli, G. Kopsinis, E. Kavouklis, L. Gabriel, and H. Giamarellou. Vancomycin levels in human aqueous humour after intravenous and subconjunctival administration. *Int. J. Antimicrob. Agents* **18**:239–243 (2001).
31. T. W. Lee and J. R. Robinson. Drug delivery to the posterior segment of the eye: some insights on the penetration pathways after subconjunctival injection. *J. Ocul. Pharmacol. Ther.* **17**:565–572 (2001).
32. W. S. Foulds, D. Allan, H. Moseley, and P. M. Kyle. Effect of intravitreal hyaluronidase on the clearance of tritiated water from the vitreous to the choroid. *Br. J. Ophthalmol.* **69**:529–532 (1985).
33. B. A. Berkowitz, C. A. Wilson, P. S. Tofts, and R. M. Peshock. Effect of vitreous fluidity on the measurement of blood-retinal barrier permeability using contrast-enhanced MRI. *Magn. Reson. Med.* **31**:61–66 (1994).
34. T. L. Jackson, R. J. Antcliff, J. Hillenkamp, and J. Marshall. Human retinal molecular weight exclusion limit and estimate of species variation. *Invest. Ophthalmol. Vis. Sci.* **44**:2141–2146 (2003).
35. B. A. Berkowitz, P. S. Tofts, H. A. Sen, N. Ando, and E. de Juan Jr. Accurate and precise measurement of blood-retinal barrier breakdown using dynamic Gd-DTPA MRI. *Invest. Ophthalmol. Vis. Sci.* **33**:3500–3506 (1992).
36. N. Alikacem, T. Yoshizawa, K. D. Nelson, and C. A. Wilson. Quantitative MR imaging study of intravitreal sustained release of VEGF in rabbits. *Invest. Ophthalmol. Vis. Sci.* **41**:1561–1569 (2000).
37. H. Kim, M. R. Robinson, M. J. Lizak, G. Tansey, R. J. Lutz, P. Yuan, N. S. Wang, and K. G. Csaky. Controlled drug release from an ocular implant: an evaluation using dynamic 3-dimensional magnetic resonance imaging. *Invest. Ophthalmol. Vis. Sci.* **45**:2722–2731 (2004).
38. A. F. Holleman and E. Wiberg. *Inorganic Chemistry*, Academic Press, New York, 2001, Ch. 20.